A nanometer resolution wearable wireless medical device for non invasive intracranial pressure monitoring

Rodrigo de A. P. Andrade, *Member, IEEE*, Helder E. Oshiro, Caio K. Miyazaki, Cintya Y. Hayashi, Marcos A. Morais, Rodrigo Brunelli and João P. Carmo

***Abstract*—The non-invasive intracranial pressure (NIICP) method based on skull deformation, has been proven to be a significant tool for assessment of the intracranial pressure (ICP) and compliance. Here we present the development and characterization of a novel wireless sensor that uses this method as its working principle and was designed to be easy to use, to have high resolution, and good accessibility. Initially, a brief review of physiology fundamentals of ICP and the historic evolution of the NIICP method are mentioned. Then, the sensor architecture and the rationale for chosen components is presented aiming to ensure: nanometer displacement measurements, conversion of analog resolution to digital in high speed, fewest distortions, wireless communication, and signal calibration. The NIICP signal has a typical amplitude of 5 μm, so a resolution of at least 1% of this amplitude is required for NIICP waveform analysis. On the characterization section we demonstrate the 40 nanometer (nm) resolution of the sensor using a nanometric displacement test system that can also respond dynamically for NIICP signals from 50 beats per minute (bpm) to 180 bpm without any significant distortion (maximum deviation in P2/P1 ratio of 2.6%). The future applications for this device are broad and can enhance clinical assessment of intracranial dynamics.**

***Index Terms*—Non-invasive intracranial pressure, intracranial pressure, intracranial compliance, skull deformation, medical device, wireless sensor, wearable sensor, nanometer resolution, displacement sensor.**

I. INTRODUCTION

Innovation applied to neurology and neurosurgery advanced in the 1970's with the invention of computed tomography (CT) scan and magnetic resonance imaging (MRI) [1]–[5]. Many other instruments were developed since then incorporating new technologies to medical care, such as catheters for cerebral metabolic analysis [6], stereotactic surgical system [7], [8], intraoperative neurophysiological monitoring [9], [10], diffuse tensor imaging with fiber tractography [11]–[13], bispectral index [14]–[16], near-infrared spectroscopy monitoring [17], [18], transcranial doppler (TCD) ultrasonography [19], [20], etc.

But these medical specialties always had the challenge of accessing and assessing the intracranial compartment in regards to the Monro-Kellie doctrine [21], [22]. This well-established doctrine takes into account the dynamic balance between three major components of the central nervous system (CNS): parenchyma - cerebral and spinal cord tissues; blood - arterial and venous; and cerebrospinal fluid (CSF). It states that the sum of all components' volumes is constant, therefore, any increase in volume of one intracranial component would implicate in a decrease of another in order to maintain the equilibrium inside the restricted space delimited by the rigid bone structure (skull and vertebral canal) as a compensatory mechanism [21]–[24].

This concept also involves changes in the pressure regimen of this confined compartment considering any intracranial volume variations that normal physiological mechanisms could not compensate [24]–[27]. It would presume, then, that the bone structure is not compressive nor elastic.

Situations where intracranial pressure (ICP) is higher than normal are common in traumatic brain injury, stroke, tumors, hydrocephalus, and many other medical conditions [28]–[31]. Intracranial hypertension is often an emergency situation that can cause severe impairments and even death. It requires assertive intervention from the healthcare professionals [28], [29], [32], [33]. For this reason, the more information they have on brain functioning, the better for making adequate

Manuscript received Month XX, 2021; revised Month XX, 2021; accepted Month XX, 2021. Date of publication Month XX, 2021; date of current version Month XX, 2021. The associate editor coordinating the review of this article and approving it for publication was YYY.

This work was supported by brain4care© - Braincare Desenvolvimento e Inovação Tecnológica S.A.

R.A.P. Andrade, H.E. Oshiro, C.K. Miyazaki, M.A. Morais, R. Brunell are with enginnering departament of Brain4care, Sao Carlos, SP, Brazil. (e-mail: rodrigo.andrade@brain4.care; helder.oshiro@brain4.care; caio.miyazaki@brain4.care; marcos.morais@brain4.care; rodrigo.brunelli@brain4.care)

C.Y. Hayashi is with research departament of Brain4care, Sao Paulo, SP, Brazil. (e-mail: cintya.hayashi@brain4.care)

J.P. Carmo is with Electrical and Computer Engineering Departament, University of São Paulo, São Carlos, SP, Brazil. He is supported by a CNPq scholarship with the reference 304312/2020-7i. (e-mail: jcarmo@sc.usp.br)

therapeutic decisions.

Traditional methods of ICP monitoring require surgical intervention or other invasive procedures, such as drilling a hole in the skull to insert a catheter or inserting a needle into the spine [29], [30], [34]. These are considered gold-standard procedures for ICP direct measurement. However, there are some risks associated with them including direct lesion to the brain tissue, hemorrhages, and infection. Some other pitfalls include catheter occlusion or migration, and loss of calibration [30], [34]–[36]. All these procedures require admission to a healthcare facility restricting the use of ICP information to certain hospital units and conditions.

Additionally, it is not always feasible to use invasive ICP (IICP) monitoring for patients with risk of coagulopathy or other conditions in which the risks of using the invasive device may outweigh the benefits [37]–[39].

Even conventional imaging exams, e.g. CT scan and MRI, only bring stationary aspects from inside the cranium and sometimes do not reflect the complex kinetics between components and/or its active tensile compensatory mechanism [40].

In this context, non-invasive methods were developed in the interest of enhancing neurological assessment [30]. For instance, the ultrasound applied to neuroscience brought the TCD as a portable tool to assess the cerebral blood flow (CBF) [20], [41], [42] that supplies oxygen and nutrients for CNS. Another example would be the optic nerve sheath diameter measurement [43], [44] that can indicate an increase in ICP if it is enlarged. Similarly, the tympanic membrane displacement [30], [45], [46] evaluated by the acoustic reflexes allows insights of ICP as the cochlear fluid pressure - the fluid of the inner ear - is correlated with the CSF pressure.

All of these non-invasive methods monitor ICP indirectly through natural “gaps” provided by the anatomy and also take into consideration the Monro-Kellie doctrine limitation.

In contrast, technological advancements allowed researchers to take a step back and study the bone limitation itself defying the doctrine [47]. Reviewing basic materials physics and engineering concepts, a very sensitive equipment was able to monitor the expansion of the skull promoting new strategies to assess intracranial compartment kinetics with less clinical risks for both patients and healthcare professionals. Therefore, we describe here the development of a medical device using a nanometer resolution wireless sensor for non-invasive ICP (NIICP) monitoring based on the principles presented by Mascarenhas et al [47].

II. INTRACRANIAL PRESSURE

A. Neurophysiology

At first, it is necessary to explain the physiological aspects of CNS, its components (skull, vertebrae, meninges, CSF, parenchyma - brain and spinal cord tissues -, blood, arteries and veins), and the intracranial dynamic that supports the rationale for the development of this new equipment.

The cranium is a bone vault that holds and protects the brain tissue in the same way that the vertebral canal does with the spinal cord tissue [24], [48]. Supposedly, the bone structure was considered inelastic by the traditional doctrine [21], [22].

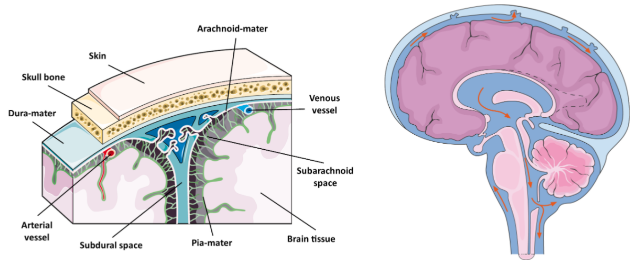

(a) Maximized cranial anatomy. (b) Illustration of cerebrospinal fluid flow.

Fig. 1: Simplified representation of central nervous system anatomy [Servier Medical Art –Modified].

The meninges are protective membranes surrounding the core of the CNS (figure 1a): 1) Dura-mater is the thicker layer closest to the internal side of the bone; 2) Arachnoid-mater is the intermediate layer with a woven-web-like structure; 3) Pia-mater is the most internal and delicate layer covering directly the brain and the spinal cord tissues. The space between the arachnoid and the pia-mater is called subarachnoid space and it is filled with CSF [27], [48], [49].

The human brain represents about 2% of the total body weight. Nonetheless, it takes in 15% of the cardiac blood supply (750-1000 mL) and consumes 20% of the total body oxygen (O2) metabolism. These numbers show a great energetic demand by the neuronal activity requiring a constant blood flow of about 45-55 mL per 100 g of nervous tissue per minute [24], [27], [49].

For this, cerebral vessels have specific anatomical characteristics and physiological properties that can change diameter instantaneously reacting to adverse health conditions, defining cerebral vascular resistance (CVR). There are two mechanisms - known as cerebral autoregulation - that involve these vascular adjustments to maintain optimal cerebral perfusion [24], [27], [49]. Cerebral arterioles are able to control CBF either dilating when systemic blood pressure is low, or constricting when it is high.

The cerebral venous blood is drained by the venous sinus of dura-mater, and superficial and deep veins along the cortex. These veins are unprovided with valves and have larger diameter than the cerebral arteries contributing to its slow blood circulation. The drainage, then, occurs due to negative thoracic cavity pressure, gravity itself and arterial pulsation [27], [48], [49].

For this reason, cerebral perfusion pressure (CPP) and CVR are key variables to determine the CBF. The CPP is calculated by the difference between mean arterial pressure (MAP) and cerebral venous pressure (CVP). Basically, it would be the adequate pressure of the incoming blood that guarantees sufficient oxygen and energetic supply. There are many difficulties to measure CVP but there is a well established correlation between CVP and ICP, the latter being easily measurable [24], [49].

The ICP value can be measured either directly into the cranium with a pressure-sensitive transducer located outside the dura-mater (epidural), within the brain tissue (intraparenchymal), and in spaces filled with CSF (intraventricular, subarachnoid), either in the vertebral canal with a manometer connected to a needle if there is a lumbar puncture (subarachnoid space) [49]–[51].

The CSF is a clear and homogeneous fluid considered an ultrafiltrate of the blood plasma. Its total amount is estimated to be 140-150 mL approximately. It is secreted by proliferations of arterioles inside the lateral ventricles, the choroid plexus. At each cardiac cycle, the blood influx generates small amounts of CSF that spread along the lateral, third and fourth ventricles, then to the aqueduct of Sylvius and, finally, to the subarachnoid space down the vertebral canal (figure 1b). It is this pulsatile distribution that can be translated into a waveform similar to the way of the blood pressure waveform [24], [27].

Considering the fundamentals of Hydrostatic (Pascal's law), the pressure in the leveled interconnected spaces filled with CSF is the same along the neural axis despite the point of measurement. Values of ICP are commonly registered in mmHg and cmH_2O [24], [27], [49]. Thus, there is a norm to use MAP and ICP to calculate CPP (CPP = MAP - ICP).

Since the parenchyma, the CSF, and the blood content are confined to the CNS compartment, any mass-effect lesion inside the cranium - e.g. tumor, hematoma - would deploit limited amounts (compensatory reserve) of CSF to the vertebral canal through the subarachnoid space and of venous blood content to the thoracic cavity by the jugular vein, due to their lower resistance, as an attempt to compensate the intracranial volume and, consequently, the pressure within [21]–[24], [52].

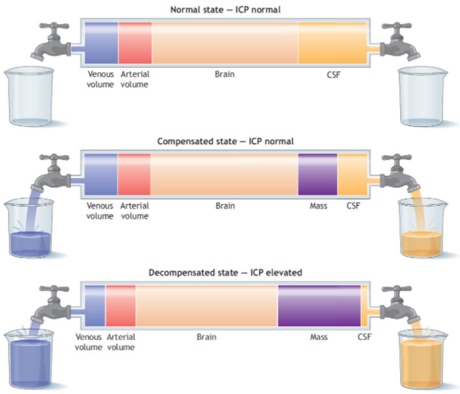

Fig. 2: Compensatory mechanism of ICP [Advanced Trauma Life Support - ATLS®].

Sustained values above 20 mmHg are considered elevated ICP and once the compensatory mechanisms reach its capacity, the pressure gradients inside the cranium can lead to herniations, shifting parts of the brain parenchyma. This dislocation is life-threatening and ends up compressing vessels, nerves and the proximal part of the spinal cord that controls vital functions (brainstem) [51], [53]. The concept of these compensatory limits is related to the exponential intracranial pressure-volume relationship and it is commonly referred to as intracranial compliance [54], [55].

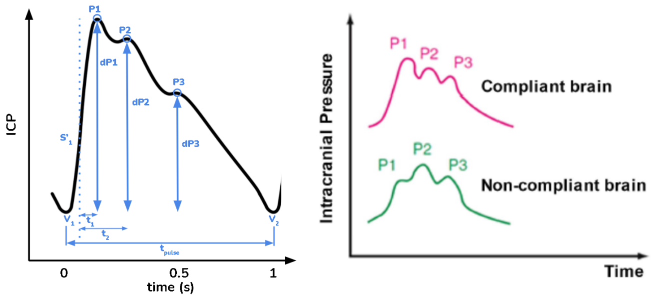

(a) ICP Waveform morphology features extracted from mathematical analysis.

(b) Depiction of ICP Waveforms between Compliant and Non-Compliant Brains.

Fig. 3: ICP waveform analysis.

B. ICP waveform parameters

Besides the absolute value presented by ICP monitoring devices, the pulsatile nature of ICP and its derivation from MAP brought to light the studies about the pulse waveform characteristics in the same way that arterial blood pressure is analyzed [56]–[59].

It is described that the ICP waveform morphology itself is a significant tool for evaluating intracranial hypertension and intracranial compliance [25], [26], [29], [60], [61]]. The ICP pulse waveform, so far studied with the invasive method, can be characterized by some of the following items [62]–[66] (Figure 3a):

- Waves: P1 (Percussion wave, due to arterial pressure being transmitted from the choroid plexus to the ventricles) , P2 (Tidal wave, related to intracranial compliance), and P3 (Dicrotic wave, related to the closure of the aortic valve during diastole);
- Amplitude of wave peaks: dP1 (relative amplitude of percussion wave), dP2 (relative amplitude of tidal wave), dP3 (relative amplitude of dicrotic wave);

Under normal ICP conditions, the amplitude of these peaks is such that $P1 > P2 > P3$ and the time elapsed (lag) from the beginning of the pulse waveform until the highest peak is shorter. When compensatory mechanisms are working properly these peak proportions maintain the same, even if there is a volume or pressure change inside the cranium, representing a compliant brain. However, when ICP reaches critical levels or volume expansion exceeds compensatory reserve, the pulse waveform morphology changes disclosing an increase of P2 peak amplitude over P1, and the lag until the highest peak gets longer [67], [68] (Figure 3b).

The lag of mechanical propagation of CSF throughout the CNS is also called latency, “upstroke time” or “time to peak” in the literature [65], [69]–[73]. To calculate time to peak (TTP), the pulse max slope S' is identified (moment in time when pulse slope is steepest) which is statistically the most stable reference point (technical parameter), and then the duration from S' to the highest pulse amplitude is marked. The normalized TTP - relation between TTP and the total pulse duration - helps interpret when the highest peak of a pulse happened, independently from the heart rate. If the TTP is longer, the highest peak is likely to be a P2 (ICP tidal wave).

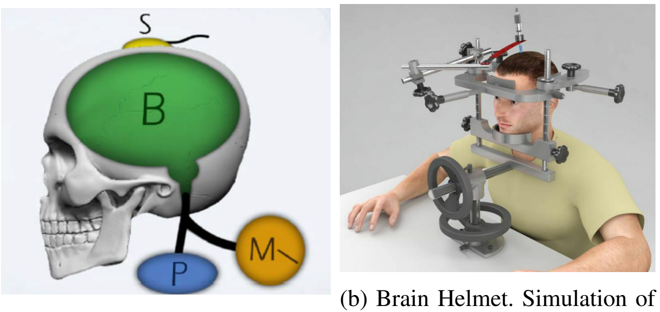

(a) First system to measure bone deformation [47]

(b) Brain Helmet. Simulation of positioning and experiments in the skull [74].

Fig. 4: First experiments evolving NIICP method.

On the other hand, if the TTP is shorter it is likely to be a P1 (ICP percussion wave). Figure 3a illustrates these parameters.

In spite of absolute ICP values, the healthcare professionals can monitor neurological conditions with waveform morphology information related to intracranial compliance. Unfortunately, there were not many medical devices that could bring such detailed information in an easy way outside clinical research protocols [65], [69]–[73].

So based on the bedside accessibility challenge, the Monro-Kellie doctrine breakthrough, and the instigating waveform morphology information, the development of an innovative NIICP monitoring device is described below presenting the mechanical method with the hardware and software elements.

III. NON INVASIVE ICP METHOD - SKULL DEFORMATION

The NIICP method based on skull deformation initiates with the proof that the skull is not a non-deformable structure and can be used as a physical parameter for the detection of changes in intracranial volume and pressure, these being governed by a constitutive relation [47].

A. Historic evolution of the method

The first experiment of this method is described by Mascarenhas et al. [47], where a deformation sensor (strain gauges) was applied to the parietal region of a human skull in a laboratory environment, confirming that ICP variations have an almost linear correlation with cranial deformation. Figure 4a demonstrates the experiment setup which simulates ICP changes by inflating a balloon inside the skull and the attached strain gauge sensor was able to measure deformations on the bone surface.

Expanding this hypothesis, further *in vivo* experiment Vilela et al. [75] validated the method comparing it to the standard IICP, known as minimally invasive ICP monitoring method. In this experiment, strain gauge sensors were externally glued onto the exposed skull of rats and saline was infused into the vertebral canal to induce ICP changes. The skull deformation captured by the strain gauge had a high positive correlation with direct IICP values (Pearson's correlation coefficient r = 0.8±0.2, with a range of 0.31–0.99).

Since then, some concepts were developed seeking to measure this skull deformation in a practical way. Andrade (2013) [74] cited a stereotactic apparatus called *Brain Helmet* (Figure 4b) with cantilever beam, fixed strain gauges, and a pin touching the patient's head to capture the skull expansion. This device, however, had difficulties in keeping the patient's head resting still. The evolution of these concepts brought better results when the cantilever beam and strain gauges (Figure 5a) were embedded in a support and enclosured, enabling the wearable format on a headband (Figure 5b) [74], [76]. This way, the sensing mechanism used the patient's own head as a relative reference instead of a fixed reference frame like the table used in *Brain Helmet*.

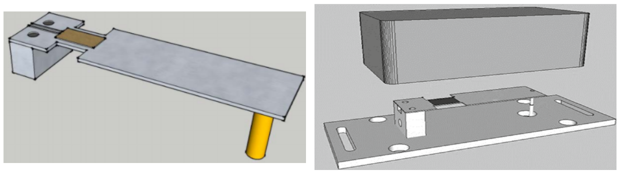

(a) Cantilever beam

(b) Schematic drawing

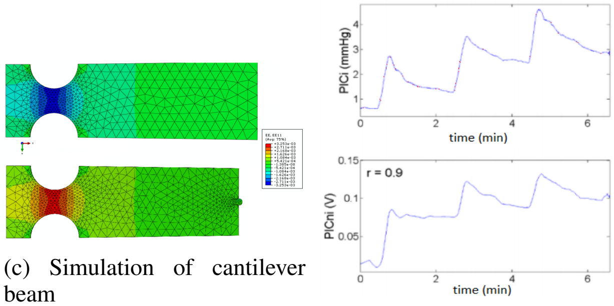

(c) Simulation of cantilever beam

(d) Result comparing IICP and NIICP

Fig. 5: (a) Cantilever beam with touch pin and strain-gauge.(b) Schematic of main components of non-invasive sensor within the plastic housing: A) support for sensor bar; B) strain gauge sensors; C) sensor cantilever bar; D) pin. (c) Simulation of stress concentration of cantilever bar. (d) Experiment of three saline infusions in rats.

The skull expansion signal was indeed captured by the sensor but each pulse had a high noise-signal ratio, though. An improvement in the system's signal acquisition and sensor's instrumentation by designing a stress concentration in the cantilever beam (Figure 5c) allowed evident amplification of NIICP signal on waveform morphology of animal experiment [74], pretty similar to the IICP sensor waveform (Figure **??**.

The study of Frigieri et al (2018) [77] used the refined NIICP method in patients with traumatic brain injury. They compared the NIICP with the IICP sensors and invasive arterial blood pressure (ABP), and found great similarities between NIICP and IICP much more than the ones found between NIICP and ABP. Nevertheless, none of the studies mentioned [74]–[76] could establish a direct relationship between NIICP and absolute values of IICP.

These NIICP studies [74]–[76] [77] presented good evidence that the method is strong in ICP waveform analysis, allowing the development of a medical device applying the non-invasive assessment of intracranial dynamics and compliance commercially. The transducer working principle (subsection III-B) of the first NIICP wired sensor (Model BcSs-PICNI-2000, Braincare Desenvolvimento e Inovação Tecnológica

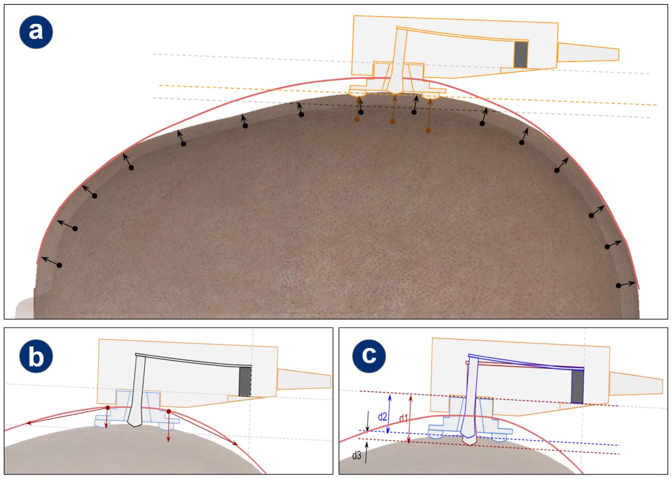

Fig. 6: Sensor working principle. (a) Amplify representation of skull expansion (b) Headband fixing forces (c) Displacement transducer of skull expansion.

S.A., Sao Carlos, Brazil) launched commercially in 2017 is also applied to the current wireless version described below (Model BcSs-PICNIW-1000, Braincare Desenvolvimento e Inovação Tecnológica S.A., Sao Carlos, Brazil).

B. Working principle

The sensor's principle of operation is fundamentally based on the studies previously described in subsection III-A. The physiological skull expansion phenomenon starts in the heart, which pumps blood to the brain through arterial vessels. Inside the head, these vessels expand in diameter and cause intracranial volume and pressure variations. Then the skull experiences small deformations due to these volume and pressure variations (as illustrated in an amplified manner in Figure 6.a). By fixing a headband (red line of Figure 6.b) with a certain tension, so that the sensor's pin touches the head and keeps the device in the lateral of the head just above the ears (frontotemporal region), the skull deformations can be perceived as displacements in the pin which bends the sensor's cantilever beam. Figure 6.c illustrates the displacement perceived by the sensor, where the resulting displacement (d_3) is the difference between initial position (d_1) and final position (d_2), $d_3 = d_1 - d_2$, fixing sensor's support bar as a reference.

When the cantilever beam bends it causes tension and compression on the fixed strain gauges. The strain gauges in full bridge Wheatstone configuration amplify the mechanical signal and convert to proportional electrical signal (related to resistance variation) that is readed by an analog signal acquisition system (e.g. multiparameter patient monitor). The working principle is summarized by the block diagram in Figure 8 on groups 1 and 2, where each block is a physical behavior which leads to the next block. The group 1 of blocks (physiology group) are the biological events series that cause skull deformation, and the group 2 (transducer group) is related to how the skull deformation is transduced into an analog electrical signal by the sensor.

C. Motivation

The NIICP wired sensor BcSs-PICNI-2000 demonstrated some limitations, summarized here below, that instigated the functionalities enhancement for the new wireless version:

1) *Usability*: It is a complex process to move the patient between sectors in a hospital [78] and even inside a room when a patient is being monitored. The sensors are connected to a multi-parameter device limiting mobility depending on the length of cables and bed layout.
2) *Monitor compatibility*: BcSs-PICNI-2000 sensor was developed to be compatible with all patient monitors available on the market that have invasive pressure input and are in accordance with ANSI AAMI BP22 [79]. However, some models of patient monitors do not display the waveforms with minimum resolution and span necessary for visualization and analysis by the health professional with quality.
3) *Report generation*: To generate reports of waveform analysis it was necessary to record the data from the monitor and then upload manually for data processing. An integrated and automatic system between sensor and cloud would make this process easier.
4) *Instrumentation sensitivity*: The cantilever beam was designed to be very thin in order to sense very small variations of the skull expansion. Unfortunately, some operators overloaded the instrument when handling it during positioning and tightening in the patient's head, causing plastic deformation in the bar.

IV. THE WIRELESS SYSTEM, ARCHITECTURE AND SENSOR DESIGN

The brain4care® Wireless System (BWS) is the evolution derived from the wired system and provides NIICP waveform information for interpretation. This medical device is intended to monitor variations in ICP of patients with suspected ICP alteration or changes in intracranial compliance.

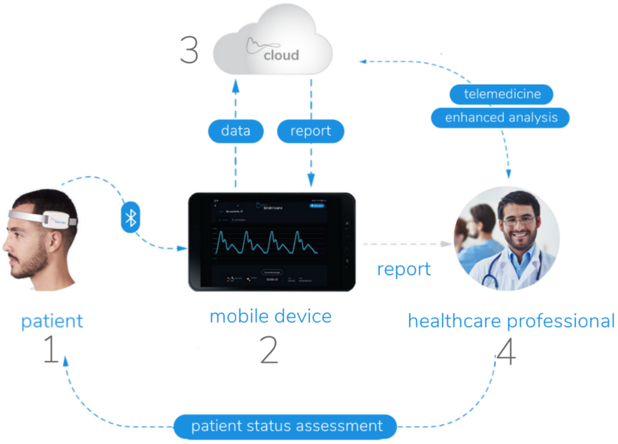

Fig. 7: The brain4care system.

The figure 7 represents the system functionality and the overall data journey. The sensor 7.1 contains a high resolution acquisition electronics, its battery powered continuously transmits the NIICP signal to a mobile application (mobile

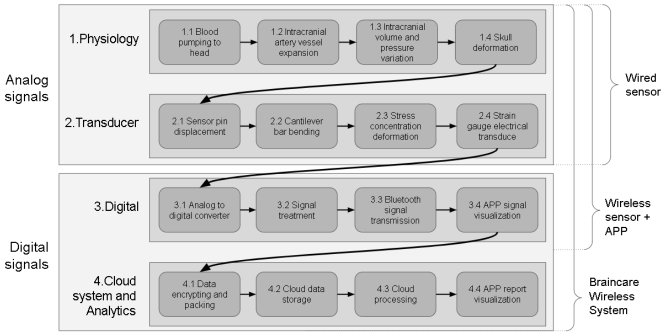

Fig. 8: Signal journey. From blood flow to report analysis block diagram.

app) 7.2 via proprietary protocol over Bluetooth® connection for clinical assessment in real time and, afterwards, data is sent to the cloud 7.3 via HTTPs connection on the mobile app. The analytical software inside the cloud includes data parsing, detrending, signal validation, signal filtering, inversion verification, pulse identification, artifact removal, pulse alignment, pulse averaging, and pulse parameters calculation. The processed information is sent back to the mobile app in the form of a report with the waveform image and additional information. There is also the possibility to visualize the waveform directly on the patients monitor's screen by plugging in a wireless receiver through the invasive pressure input.

The mobile app displays the following information to the healthcare provider 7.4 for interpretation: real-time ICP waveform visualized on either the mobile device or the connected patient multi-parameter monitor, preliminary and final reports with estimated P2/P1 ratio variation through time, ICP waveform signal over time, pulse morphology as average per minute with P2/P1 ratio, number of useful pulses, heart rate (bpm), and TTP.

Additionally to the wired sensor and analog signals explained in Section III (groups 1 and 2 of diagram blocks), Figure 8 also includes the BWS implementations and signal journey (groups 3 and 4 of Figure 7). Group 3 starts with the digitization of analog signals (3.1), which leads to signal treatment (3.2) with filtering, error compensation and voltage to micrometer calibration. Then the NIICP signal is sent to the APP (3.3), where it can be visualized (3.4). Group 4 involves the cloud and analytics processes of report generation.

A. brain4care sensor architecture and design

The brain4care® wireless sensor comprises a mechanical transducer with the same principle of the wired sensor (described in Section III) to capture nanometric skull displacements, and embeds a high resolution and high speed analog to digital converter.

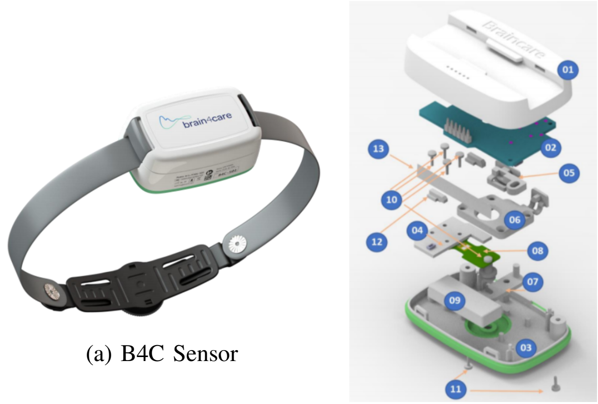

(a) B4C Sensor

(b) Sensor exploded view

Fig. 9: (a) Wireless sensor assembled. (b) 01 - Top sensor housing, 02 - Main PCB, 03 - Bottom sensor housing, 04 - Instrumentation PCB, 05 - ON-OFF Switch, 06 - Mechanism cover, 07- Contact pin lock, 08 - Cantilever beam, 09 - Internal battery, 10 - Contact pin screw, 11 - Sensor screws, 12 - Sensor travel limiter, 13 - Bluetooth antenna

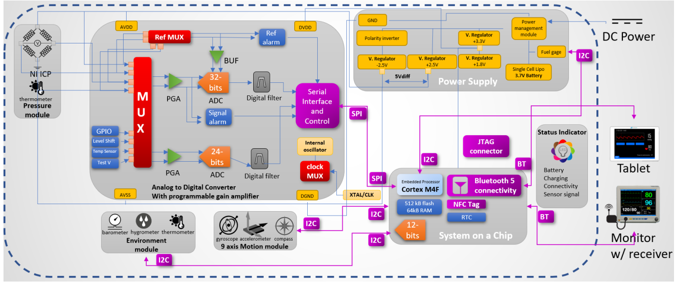

Fig. 10: Block diagram of the wireless sensor architecture

B. Displacement Transducer

The displacement transducer is based on a cantilever beam embedded on the bottom of the sensor. The cantilever beam (9b.08) has a rectangular shape with dimensions of approximately 36x13x0.38mm and is made with a beryllium copper alloy that has excellent properties for load cell instrumentation, presenting excellent mechanical properties. There is an isostress concentration to increase the sensitivity that mechanically amplifies up to 3 times the deformation in an homogeneous way over the sensitive region, where double uniaxial strain gauges are glued on each side of the beam forming a full Wheatstone bridge.

C. Hardware e Firmware

Figure 10 represents the hardware functionality of the wireless sensor. Unlike the wired sensor, the wireless one sends the waveform signal to mobile devices or receivers on patient's monitors and it is now responsible for the entire analog front end, analog to digital conversion, compensation of external effects, filters, electrical signal for displacement calibration.

The analog front end of the NIICP signal is initially composed of a full Wheatstone bridge with compensations of zero, span, and thermal drifts related to cantilever dilation and strain gauges unbalance. The voltage excitation of the bridge is also controlled to ensure the relative reading of the signal. A 32-bit delta-sigma ADC digital analog converter with differential input and programmable gain amplifier (PGA) is responsible for converting the electrical signal from the sensor already compensating for the relative signal in μV/V. A 24-bit ADC converter is dedicated for reading the sensor temperature for thermal compensation.

Digital filters of 4th and 5th order are present to guarantee the signal quality against external noises. For this purpose, the system uses two methods to ensure the signal quality against noises. The first would be the rotation of the positive and negative pins, in signal reading, to reduce the voltage offset drift, this method reduces the noise by a factor of 1.4. The second method is a digital filter, that can be described as a function $(sin(x)/x)^n$, where n is the filter order and x is the analog signal value.

Processing is made by Nordic® Semiconductor's System-on-Chip(SoC) nRF52832 which supports Bluetooth® 5.2. It is built around an Arm® Cortex ™ - M4 CPU with floating point unit running at 64 MHz, 512 KB Flash + 64 KB RAM. The communication between the SoC and the peripherals is made by high speed serial communication. A set of inertial and environmental sensors provides more information and intelligence for compensation of the acquired signal against environmental and inertial effects. Table II includes the main general specifications of the sensor.

The sensor's firmware is responsible for executing the communication between the processor, the peripherals and exchanging messages using the proprietary protocol over Bluetooth® LE 4.0 or 5.0 (1.0 Mbps or 2.0 Mbps), depending on the compatibility of the mobile device. It controls the acquisition, conversion, filter and compensation of the NIICP signal waveform using the digitized signals from the main sensor and accessories. The sensor firmware update is done by DFU-OTA through the brain4care® app.

D. Mechanical enclosure and materials

The cantilever beam is very sensitive even against small efforts ($>> 400g$), so the internal construction of the sensor was designed to provide mechanical protection for it against overloads during usage and transportation. The system is equipped with travel limiters active during operational use and other mechanism locks to avoid shocks caused by transporting the sensor. When the sensor is turned off, the sliding button (9b.05) activates the locking mechanism (9b.07) preventing the contact pin from transferring effort to the beam. When turned on, the system releases the sensor pin for movements in the direction of the cantilever. Moreover, the system has a stroke limiter (9b.12) that allows 1.5 mm maximum deflection excursion of the beam. Simulations during product development showed that, with the current beam design, excursions over 2 mm shorten the sensor's life to up to 10,000 cycles. With the 1.5 mm limitation, the life cycle due to large displacements is in the order of 10^9 cycles, making product life practically infinite when related to the number of monitoring. These large displacements can occur when the headband is overtightened and the sensor is pressed on the patient's head.

V. MANUFACTURING TESTS AND CALIBRATION PROCESS

An Electronic Automatic Sensor Testing System (called SETAS) was exclusively designed by the engineering team to perform different analysis including calibration, sensitivity, and other electrical and mechanical tests. It is basically a linear stage (moving table) that can perform programmed nanometric resolution dynamic displacements powered by a full data acquisition system that captures precise measurements of main variables generating reports for calibration and traceability.

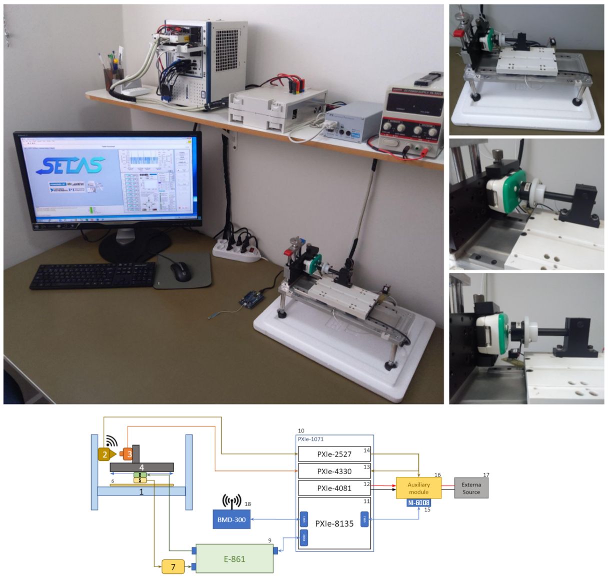

Fig. 11: SETAS system test assembled and connection diagram

A. Hardware

In order to induce movement/displacement on the sensor, the SETAS slides over a busbar through bearings, using a N-310 NEXACT® from Physik Instrumente (Physik Instrumente (PI) GmbH Co. KG, Germany) as a linear actuator, which is controlled by a PiezoWalk® NEXACT® controller model E-861 from the same manufacturer. The actuator has 125 mm of travel range, Force generation up to 10N and can reach 0.03nm of resolution. The E-861 can be commanded by RS-232 or USB interface. The movement is mainly closed-looped with the aid of an optical encoder model TONiC T-1011-30A, and a micrometric scale RSLM-SS-20U3A-0100-A, both from Renishaw™. For actuator referencing, the system also uses a load cell model FC2211 from TE Electronics. The scale has 20 nm of LSB (Less Significant Bit), limiting the closed loop control to fine setpoints. For more refined displacements, an open-loop can be used.

The overall system and its assembly can be seen in 11. The full SETAS specification is shown on Table I.

This setup allows a complete portfolio of static and dynamic bench tests to know the conditions of the sensor instrumentation and its behavior, as well as to identify the electrical and functional characteristics of the sensor's main board.

B. Software

The SETAS software was fully developed in LabVIEW from NI and designed to perform both manual readings and also prepare routine sets that can be executed automatically.

These routines are structured as tests and subtests, which are processed in a determined sequence. Each test type has its own execution parameters. The main routine that standardizes all sensors is the calibration procedure.

VI. CHARACTERIZATION OF THE SENSOR

The wireless sensor was characterized in 4 sections:

TABLE I: SETAS specification

Parameter	Value
Linear Actuator:	
Controller:	
Manufacturer	Physik Instrumente-PI
Model	E-861.1A1 NEXACT
Power supply	24V, 42W
Communication	RS-232/USB
Interpolation rate	1000
Encoder read resolution	20nm
Encoder reading rate	100S/s
Position writing rate	100 writings/s
Linear Drive:	
Manufacturer	Physik Instrumente-PI
Model	N-310.16 NEXACT
Push/Pull force	10N
Travel range	125mm
Open-Loop resolution	1nm (with E-861)
Operation voltage	-10 to +45V
Travel range in analog operation	7um
Max. speed	10mm/s
Scale:	
Manufacturer	Renishaw
Model	RSLM-SS-20U3A-0100-A
Length	130mm
Readhead	
Manufacturer	Renishaw
Model	T-1011-30A
SDE (typical)	30nm
Max. speed	10m/s
Interface:	
Manufacturer	Renishaw
Model	TI0000A00A
Output Type	Two differential sinusoids in quadrature
Period	20um
PXI:	
Manufacturer	National Instruments
Chassi Model	PXIe-1071
PC Controller Model	PXIe-8135
DMM Multimeter Model	PXIe-4081
Bridge Model	PXIe-4330
Multiplex Model	PXI-2527

- **Sensor specification:** technical specifications of the project and performance of the electronics that composes the sensor
- **Sensor precision:** test that indicates the stability of measurements, repeatability and reproducibility among different sensors in the working range
- **Sensor sensitivity:** test that indicates the minimum change in the input that the sensor can detect
- **NIICP waveform characteristics reproduction:** a comparison between the characteristics of the waveform performed by SETAS at the sensing pin and the characteristics of the waveform perceived by the sensor

A. Sensor specification

Table II provides a summary of the specifications of the B4C wireless sensor and its main components. The peak to peak noise of the ADC (0.737 μVpp) is equivalent to 51.59 nm when converted to displacement units considering the typical calibration coefficient of 0.35 μm/μV/V and the excitation voltage of 5 V in the instrumentation bridge.

TABLE II: Brain4care Sensor Specifications

Parameter	Value
Power Consumption Average	45 mA
Internal Battery Autonomy	5h 50m
External Battery Autonomy	21h 30m
Batteries life	500 cycles (80%)
Dimensions	73.55 mm x 44.57 mm x 32.50 mm
NIICP Sample rate	266.1 SPS
ADC ENOB with chop mode enabled	21.38 bits (18.48 free of noise bits)
ADC noise with chop mode enabled	0.099 μVrms (0.737 μVpp)
Mechanical limit	1500 μm

TABLE III: Factors that contributes to the variability of the signal

Variation factor	Components	Description of measurement
Stability	A	Variability intrinsic to the sensor. It also represents the variability of measurements once the sensor is settled.
Repeatability	B	Variability between repetitions caused by manual handling and positioning a sensor in the test system.
Reproducibility	C	Variability caused only by differences between sensors.
Total variability	A+B+C	Variability considering all factors

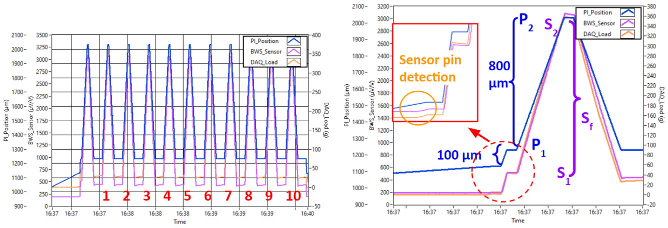

(a) Repetition cycle

(b) First measurement in a repetition cycle

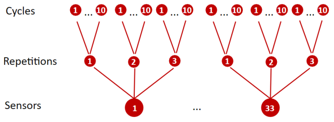

(c) Total amount of cycles

Fig. 12: (a) One repetition round. A total of 990 measurements were taken as illustrated in (c). Item (b) shows in detail the pin detection, initial offset of 100 μm and first back and forth cycle of a repetition

B. Sensor Precision

A stability and precision study involving a total of 33 sensors was performed in order to evaluate the factors that contribute to the variability of measurements, their contribution to sequential measurements and sequenced repetitions. The variation factors considered are presented and described in III.

A total of 33 sensors were tested. A test routine composed of 11 back and forth cycles of 800 µm displacements (figure 12a) was repeated 3 times for each sensor. The first cycle was not computed due to stabilization purposes. The total amount of measurements are illustrated in figure 12c.

TABLE IV: wireless sensor sources of variation and contribution

Sources of variation	**Variance (μm)^2**	**Contribution (%)**
Stability	3.107	1.11
Repeatability	181.687	64.80
Reproducibility	95.559	34.08
Total variability	280.353	100.00

TABLE V: wireless sensor sources of variation standard deviation and contribution, variability limits and percentage deviance from mean measurement

Sources of variation	**Standard deviation** (μm)	**Total Variation** (%)	**Precision Limit$_{99.7}$ (μm)**	**Deviance from mean measurement** (%)
Stability	1.763	10.53	5.288	0.66
Repeatability	13.479	80.50	40.437	5.03
Reproducibility	9.775	58.38	29.326	3.65
Total	16,744	100.00	50.23	6.24

The signal variation caused by the 800 μm variation will be calculated as $S_f = S_2 - S_1$, where S_1 and S_2 are the signal in μV/V read by the sensor. This process is illustrated in figure 12b.

The displacement measured by the sensor is be given by:

$$D = (S_2 - S_1) * (calibration\, coefficient)$$

where the calibration coefficient is the coefficient obtained for each sensor that converts the value obtained from $\mu V/V$ to μm.

The average of the 990 measurements obtained using brain4care wireless sensor resulted in 804.461μm. Table IV shows the variance of each factor and their contribution percentage.

The standard deviations obtained from the variance values and their contributions are presented in table V, followed by the precision limit, calculated as 3 standard deviation (confidence of 99,7% when considering a normal distribution of measurements) and its percentage considering the mean value of 804.461μm.

The results indicate that the main contributor of the total variability measured in this test was sensor handling and positioning in the test setup factor (64.08% of contribution). The variability in measurements due to differences between sensors was 34.08% of contribution and the variability due to variations intrinsic to a sensor is considerably smaller, with 1.11% of contribution. Also, the precision limit among all the measurements corresponds to 6.24% of the mean measurement of the range tested (804 μm), being that the main contributor of the deviation was due to the handling and positioning of the sensor in the bench setup, and the precision limit of consecutive measurements without handling or changing the sensor corresponds to only 0.66% of the mean measurement.

C. Sensor Sensitivity

In order to guarantee the quality of the waveform morphology and its parameters, the sensor is required to have nanometric resolution. The displacements must be distinguishable at a level of 1% of the cranial expansion. The sensitivity of the sensor was tested using SETAS to produce nanometric dynamic displacements against the sensitive pin of the sensor. Initially, SETAS was programmed to reproduce 10 steps of 500 nm, resulting in the total displacement of 5 μm. For this test, the closed-loop mode was used, and the displacements were controlled using the optical encoder as position feedback.

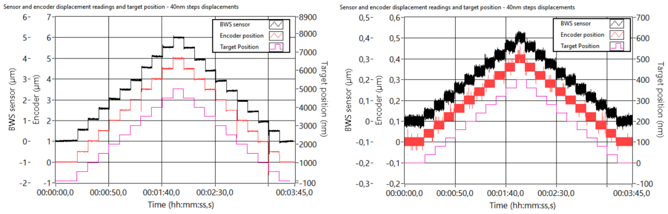

(a) 500nm steps.

(b) 40nm steps.

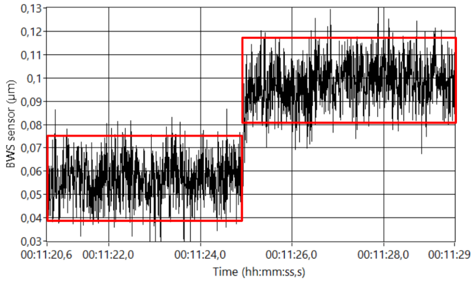

(c) Signal read by the sensor during a 40nm step and the redbox indicates the equivalent interval of 4 sigmas.

Fig. 13: (a). signal obtained from 10 displacements of 500nm (b). signal obtained from 10 displacements of 40nm (c) step of 40nm close up. The red box represents the interval of 4 standard deviations.

The initial position of the actuator before starting performing the steps was 200 μm beyond the limiar where the actuator touches the sensor's pin. The signal was detrended using a linear equation considering the initial and final position readings and scaled to match the encoder readings. The readings from B4C wireless sensor and encoder are compared in the figure 13a. The y-axes have the same span, but the limits were offset to make the plots more visible.

Next, the sensor was tested with cycles of 10 steps of 40 nm back and forth using SETAS in closed-loop mode. The encoder and B4C wireless sensor signals are shown in the figure 13b.

The change in the signal caused by a displacement of 40 nm is still visually distinguishable. The mean standard deviation in 1 second of data for all the segments in 5 cycles was 9.124nm. A confidence interval of ±3 sigmas is then equivalent to a deviance interval of ±27.372 nm in the sensor's readings, and a confidence interval of ±2 sigmas results in deviance of ±18.248nm nm. Defining the resolution as 4 sigmas, which results in a probability of 4.6% that a sample lies out of the range, during this test it was obtained a resolution of 36.496 nm. The 4 sigmas interval is illustrated in the figure 13c, where the red box height indicates the interval enclosing the signal read by the sensor between a step of 40 nm.

In order to test the sensor's response for displacements of 4 nm SETAS was configured to work in open-loop mode, since the encoder used to control the position on closed-loop mode has a digital resolution of 20 nm. In this test, displacements

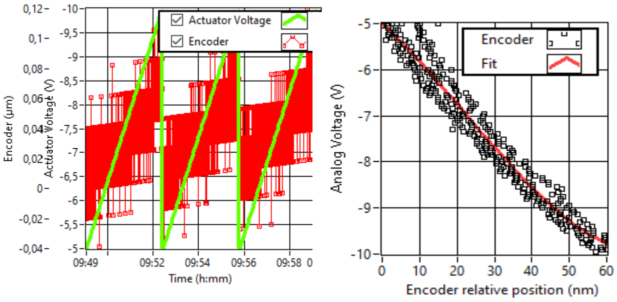

(a) Voltage applied to excite the actuator and the encoder displacement reading.

(b) Calibration curve using a third order polynomial equation.

Fig. 14: Figure (a) illustrates the voltage applied to excite the actuator and the encoder displacement reading. These data are used to obtain the calibration curve (b).

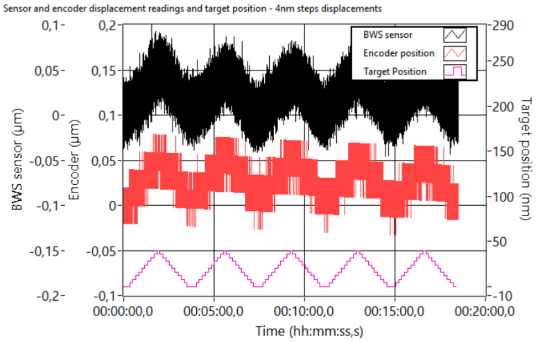

Fig. 15: Signals obtained by the sensor and by the encoder as SETAS sets the target position in 4 nm steps.

were controlled only by specifying the analog voltage that will excite the piezoelectric actuator.

Since the position is not controlled directly, a voltage to displacement calibration curve was obtained. The actuator was excited in a range of -5 V to -10 V in steps of 50 mV and 2 seconds, and the mean measurement of the encoder during the middle 1 second (100 samples) of each step was registered.

The Figure 14a shows the applied excitation voltage of the actuator and the raw readings of the encoder. Figure 8 shows the calibration curve obtained by fitting a third order polynomial equation where each point on the graph represents the mean reading of the middle 1 second (100 samples) of each step.

SETAS was programmed to perform 5 cycles of ten 4nm positive and negative steps using the polynomial equation obtained from calibration. The actuator stood still for 10 seconds in each step level. After detrending the signal using a linear equation considering equal the initial and final value of the acquisition, and scaling the obtained signal in μV/V to match the maximum amplitude obtained by the encoder in μm, the signals are presented in figure 15.

To better visualize the readings, figure 16 shows the boxplot of one of each step level cycle from both sensor and encoder readings. The data used to compute the boxplots were sequential readings in an interval of 1 second, 8.5 seconds after the step occurs. Due to the digital resolution limit of the position encoder, the first, second and third quartiles are coincident in some of the encoder readings. Also, the nuances are more distinguishable in the B4C wireless sensor boxplot. In this level, it is hard to check if the steps were performed correctly due to the encoder resolution limit.

TABLE VI: Comparison of the normal waveform characteristics based on the encoder readings and the signal obtained by the sensor

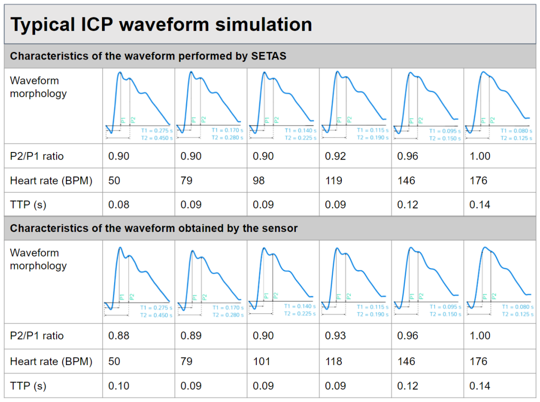

Typical ICP waveform simulation						
Characteristics of the waveform performed by SETAS						
Waveform morphology	T1 = 0.275 s T2 = 0.450 s	T1 = 0.170 s T2 = 0.280 s	T1 = 0.140 s T2 = 0.225 s	T1 = 0.115 s T2 = 0.190 s	T1 = 0.095 s T2 = 0.150 s	T1 = 0.080 s T2 = 0.125 s
P2/P1 ratio	0.90	0.90	0.90	0.92	0.96	1.00
Heart rate (BPM)	50	79	98	119	146	176
TTP (s)	0.08	0.09	0.09	0.09	0.12	0.14
Characteristics of the waveform obtained by the sensor						
Waveform morphology	T1 = 0.275 s T2 = 0.450 s	T1 = 0.170 s T2 = 0.280 s	T1 = 0.140 s T2 = 0.225 s	T1 = 0.115 s T2 = 0.190 s	T1 = 0.095 s T2 = 0.150 s	T1 = 0.080 s T2 = 0.125 s
P2/P1 ratio	0.88	0.89	0.90	0.93	0.96	1.00
Heart rate (BPM)	50	79	101	118	146	176
TTP (s)	0.10	0.09	0.09	0.09	0.12	0.14

TABLE VII: Comparison of a pathological waveform characteristics based on the encoder readings and the signal obtained by the sensor

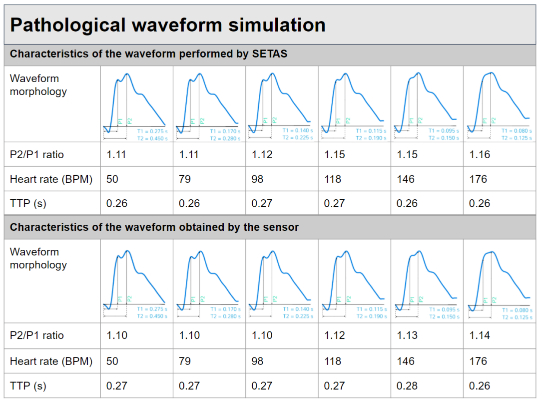

Pathological waveform simulation						
Characteristics of the waveform performed by SETAS						
Waveform morphology	T1 = 0.275 s T2 = 0.450 s	T1 = 0.170 s T2 = 0.280 s	T1 = 0.140 s T2 = 0.225 s	T1 = 0.115 s T2 = 0.190 s	T1 = 0.095 s T2 = 0.150 s	T1 = 0.080 s T2 = 0.125 s
P2/P1 ratio	1.11	1.11	1.12	1.15	1.15	1.16
Heart rate (BPM)	50	79	98	118	146	176
TTP (s)	0.26	0.26	0.27	0.27	0.26	0.26
Characteristics of the waveform obtained by the sensor						
Waveform morphology	T1 = 0.275 s T2 = 0.450 s	T1 = 0.170 s T2 = 0.280 s	T1 = 0.140 s T2 = 0.225 s	T1 = 0.115 s T2 = 0.190 s	T1 = 0.095 s T2 = 0.150 s	T1 = 0.080 s T2 = 0.125 s
P2/P1 ratio	1.10	1.10	1.10	1.12	1.13	1.14
Heart rate (BPM)	50	79	98	118	146	176
TTP (s)	0.27	0.27	0.27	0.27	0.28	0.26

D. *Waveform Characteristics Comparison*

With the aim of testing the dynamic behavior of the sensor when compared with the absolute pin deflection, two types of NIICP waveforms were simulated using SETAS and read by the sensor and absolute encoder during 3 minutes. The BWS generates reports for each waveform signal. The frequency (heart rate) of each waveform varied from 50 bpm to 180 bpm and the amplitude was constant of 10 µm. One minute of data of each waveform frequency was analysed and the parameters of P2/P1 ratio, heart rate and the normalized TTP performed by SETAS were compared to the parameters obtained by the sensor.

Due to the limitation of 100 position writings/second to reproduce the waveform, some details of the waveform morphology performed were affected when increasing the heart rate of the waveform. Nevertheless, the relation between the waveforms obtained from the encoder and sensor is still close, with the maximum deviation of parameters of 0.03 (2.6%) in the P2/P1 relation of the pathological waveform of 118

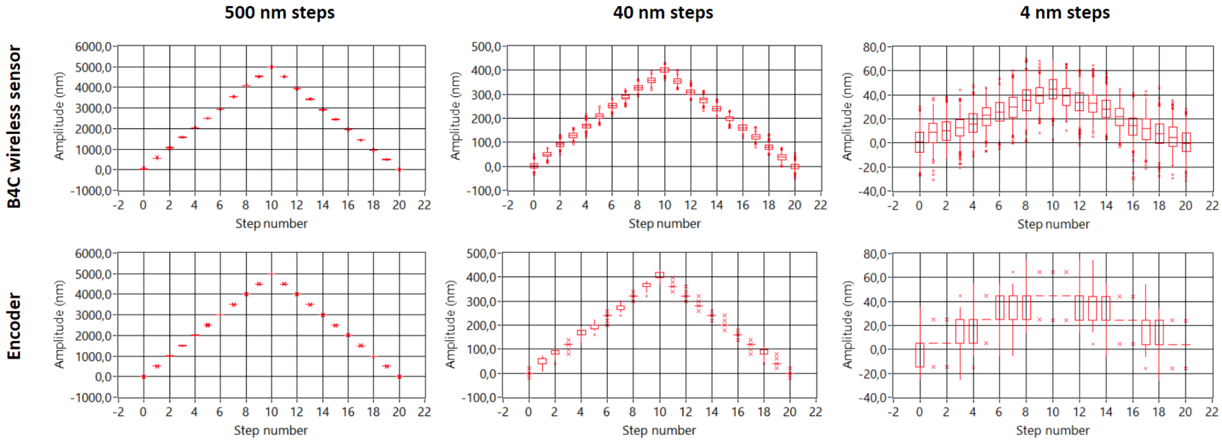

Fig. 16: B4C wireless sensor and encoder boxplot comparison for a cycle of 500 nm, 40 nm and 4 nm steps.

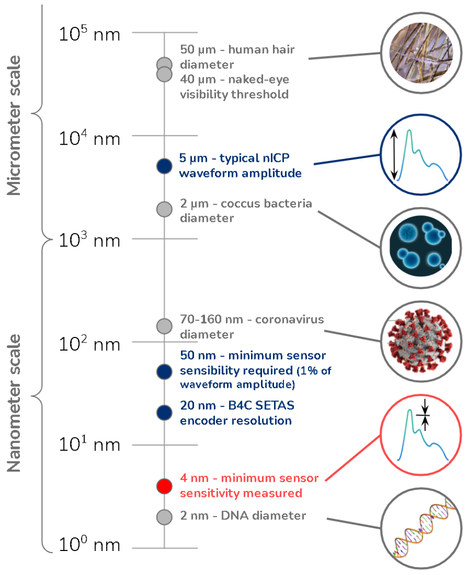

Fig. 17: Logarithm scale comparison for sensor sensitivity.

bpm. It is worth to note that there are a few elements that can contribute to the differences, including the damping that may occur between the mechanical elements of SETAS and the processing algorithms. Table VI and Table VII summarize the characteristics of the signal performed by SETAS (optical encoder) and the signal obtained by the wireless sensor.

VII. DISCUSSION

A. NIICP signal scale comparison

For comparative purposes, Figure 17 demonstrates the magnitude size of some common examples and how they compare to values analysed in this work. It is noticed that the average NIICP waveform amplitude observed by NIICP sensors based on skull expansion (5 µm) is one-tenth of a human hair diameter and below naked-eye visibility, so skull expansion can not be observed.

Furthermore, in section VI the system demonstrated excellent precision and sensibility, perceiving up to 4 nm of displacement, a scale that is comparable to a DNA diameter (2 nm). When considering noise and stability, the sensor was capable of distinguishing level differences of 40 nm with confidence superior to 95%.

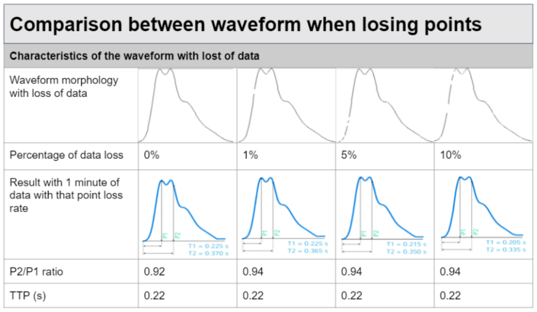

Comparison between waveform when losing points

Characteristics of the waveform with lost of data				
Waveform morphology with loss of data				
Percentage of data loss	0%	1%	5%	10%
Result with 1 minute of data with that point loss rate	P1 P2 T1 = 0.225 s T2 = 0.370 s	P1 P2 T1 = 0.225 s T2 = 0.365 s	P1 P2 T1 = 0.215 s T2 = 0.350 s	P1 P2 T1 = 0.205 s T2 = 0.335 s
P2/P1 ratio	0.92	0.94	0.94	0.94
TTP (s)	0.22	0.22	0.22	0.22

TABLE VIII: Example of NIICP waveform with data loss, the first signal without loss, the second losing 1%, the third losing 5% and the fourth losing 10% of data (randomly created).

B. NIICP waveform integrity and analysis

In addition to the current Bluetooth® standard, a proprietary Bluetooth® protocol was designed to guarantee the integrity of the communication signal and to avoid errors caused by weak signal strength between devices due to obstacles or distance. It identifies points that were lost taking into account the moment that these losses occurred, thus avoiding distortions in the original waves. The comparison between the signal is presented below in Table VIII indicating waveform data without loss of points, with 1% loss, with 5% and 10% loss.

The results show that even losing 10% of points, in the average of the minute, the NIICP waveform characteristic almost doesn't change. Tests checking for data loss on the BWS were executed to explore critical scenarios beyond the ones specified for its use. Signal acquisition was performed five times, each with 1-hour duration, with three different sets of equipment, at a 15-meters distance between sensor and receiver inside a closed environment. Monitoring sessions showed that waveform integrity had less than 1% of data loss even at distances three times further than the originally recommended, ensuring signal quality.

C. Wireless sensor contributions

Some improvements and contributions of wireless sensor is described below:

1) *Signal confiability*: By calibrating into displacement measures, the wireless sensor improves the reproducibility of the system, making it possible to compare the results between sensors and patient monitorizations. Besides, considering the resolution as a level difference that is distinguishable 95.4% of the time or more, the goal of less than 1% of typical NIICP signals resolution was reached, as demonstrated in tests of section VI. Furthermore, no post-process filtering was used during the sensitivity test, indicating that a better signal can be achieved without compromising important information, typically under 18Hz.
2) *Usability*: Compared with the wired sensor, the wireless sensor is: easier to use, enhances mobility, makes positioning easier, has less risk of failure, and has less patient discomfort.
3) *Integration with other systems*: Wireless able to communicate in real time with patient monitors and mobile device applications simultaneously, making possible multiple usage applications. Besides that, cloud integration generates reports faster than the previous system, and allows physicians to access them remotely.

D. Limitations and opportunities

The device presented here brings light to new roads inside neurological monitoring for healthcare professionals. Improving the usability will directly affect how the user operates the sensor, reducing errors, making it more efficient, effective and then increasing the number of monitorizations one can produce. Nonetheless, there are still some limitations that should be considered:

1) *Operator dependency*: Like any other sensor (e.g., ECG, doppler ultrasonography sensor), the signal obtained may partially depend on the operator and his sense to distinguish if it is correctly positioned. Ways to improve the instantaneous feedback of the sensor positioning may greatly reduce the time spent adjusting the sensor in the patient and improving the signal quality at the same time.
2) *Sensor positioning and fixing*: Special care must be taken when monitoring people in a delicate condition due to the tension generated in the headband when fixing the sensor. The sensor is contraindicated and may be harmful to patients whose skull is fractured, submitted to decompressive craniectomy, suffering from head trauma or has missing portions. When considering patients with deformed skull, neonatal and premature application, not only the headband tension should be considered but also the headband should be able to adjust to the size of the head circumference. Developing alternative ways to fix the sensor will make NIICP monitoring more accessible and safer. Also, skull physics behavior in these cases may differ from the behavior observed in a totally developed and closed skull, requiring further studies.
3) *External influences*: both mechanical and electronic parts of the sensor may be affected by external influences. Patient's involuntary or voluntary motion can be transmitted to the cantilever beam mechanism that responds to displacements. The movements transmitted from the headband to the sensor's housing when the sensor is not positioned correctly can also attenuate the signal perceived by the sensor. Compensation algorithms using the embedded 9-axes IMU can be improved. Another possible motion source is the peripheral blood circulation, and a study using technologies like plethysmography could be performed to check its influence on the sensor‘s measurement. These measurements will increase the signal quality and reduce the number of data recollecting due to poor quality acquisition.
   Usually changes in the system temperature will not affect bruscally the NIICP parameters obtained, since abrupital changes in temperature are not expected in an interval of one pulse and small thermal drifts can be treated with a detrend algorithm before processing the NIICP parameters.
4) *System test limitation*: Within the SETAS, the position encoder resolution used in the test is 20nm, preventing the system from having a direct position feedback for displacements under this limit. The position reading/writing rate also impacts in the waveform morphology when simulating higher heart rate NIICP pulses. For tests beyond these limits, new methodologies or other equipment will be necessary.
5) *Sensor and headband size*: Headband and wireless sensor size are in development to monitor infants (0 to 36 months), for cephalic perimeter smaller than 40 cm. Besides this fact, the infant skull has fontanelles - membranes that separate cranial bones - that could have a different physics behavior compared to the adults (consolidated cranial vault). Monitoring children is also delicate because they have difficulties in resting still which creates artifacts and disturbances on the signal. Hence, the applications of NIICP method for pediatric population must still be validated, considering a possible compact format of the sensor and signal compensation against movement.

E. New Applications

Apart from the physical examination, healthcare professionals could support their therapeutic decisions with this low-risk device receiving real-time information to add one more piece to the clinical assessment puzzle. The possibility to monitor ICP and intracranial compliance with this new non-invasive method can enhance not only clinical practice inside and outside healthcare services but also deepen studies about conditions affecting CNS.

Some of the possibilities to mention here, in addition to the current IICP limitations [30], [34]–[39], would be improvement in quality of life of people with neurological disorders

[80], [81], differential diagnosis for migraine and other CNS dysfunctions [82]–[84]], less painful procedures for pediatric population [85], continuous follow-up of pseudotumor cerebri - condition in which there is no mass-effect lesion but the ICP is elevated - with less invasive procedures [86], and even further studies about microgravity repercussion on the CNS for spaceflights [87]–[89]. Situation, indeed, that until now were not so conducive to measure this physiological parameter in the traditional invasive way.

VIII. CONCLUSION

The Monro-Kellie doctrine break led to the development of a new way of monitoring the ICP and intracranial compliance based on the nanometric cranial expansions. A commercially available, wireless, non-invasive ICP monitoring sensor was described here in regards to the design and characterization.

The non-invasivity mitigates some risks including lesions and infections to the patient. Adding the fact that the sensor is portable and wireless, it is also very cost-accessible and easy to use. The device was approved by the Brazilian Health Regulatory Agency (Anvisa) (registration number 81157910004) and it is already in use inside some hospitals. Currently, the wired version is already FDA approved (registered under 510(K) Number K182073) and the wireless one is under its certification process. The device and the NIICP method described in this article are both patented (US-9826934 - USA; US-9993170-B1 - USA; EP2757939 B1 - Europe).

With the digitization of the signal and integration with the cloud and analytics tools, the system makes possible visualizing, recording and obtaining valuable information about brain compliance in a fast and easy way. The monitoring reports are also accessible via the internet and can be shared with authorized people, allowing the patient, physician or researcher to have a second opinion easily.

Methods for testing and validating the sensor were also developed since the specification standards available for ICP sensors aim the traditional invasive sensors. Three important competences were evaluated in the sensor: stability of measurements, nanometric sensitivity and waveform parameters reproduction. The results show that the sensor is sensitive enough to distinguish displacements in the magnitude of 1% of the amplitude of a cranial expansion pulse, making it a promising method by delivering a consistent waveform morphology to clinical interpretation.

The information presented in this paper explains the working principle of the sensor, its benefits and main characteristics, allowing researchers and physicians to understand the variable being monitored and to evaluate its use in their application.

REFERENCES

[1] C. d. C. Leite, E. Amaro Junior, and L. T. Lucato, *Neurorradiologia: diagnóstico por imagem das alterações encefálicas*. Guanabara Koogan, 2008.

[2] V. Petrik, V. Apok, J. A. Britton, B. A. Bell, and M. C. Papadopoulos, "Godfrey Hounsfield and the dawn of computed tomography," pp. 780–786, apr 2006.

[3] R. Zimmerman, W. Gibby, and R. Carmody, *Neuroimaging: Clinical and Physical Principles*, 01 2000.

[4] E.-W. Radue, M. Weigel, R. Wiest, and H. Urbach, "Introduction to magnetic resonance imaging for neurologists," *Continuum: Lifelong Learning in Neurology*, vol. 22, no. 5, pp. 1379–1398, 2016.

[5] N. K. Pinter and J. V. Fritz, "Neuroimaging for the Neurologist: Clinical MRI and Future Trends," pp. 1–35, feb 2020.

[6] B. Young, A. Kalanuria, M. Kumar, K. Burke, R. Balu, O. Amendolia, K. McNulty, B. A. Marion, B. Beckmann, L. Ciocco, K. Miller, D. Schuele, E. Maloney-Wilensky, S. Frangos, and D. Wright, "Cerebral Microdialysis," pp. 109–124, 2016.

[7] Z. Guo, M. C. W. Leong, H. Su, K. W. Kwok, D. T. M. Chan, and W. S. Poon, "Techniques for Stereotactic Neurosurgery: Beyond the Frame, Toward the Intraoperative Magnetic Resonance Imaging–Guided and Robot-Assisted Approaches," pp. 77–87, aug 2018.

[8] D. A. Orringer, A. Golby, and F. Jolesz, "Neuronavigation in the surgical management of brain tumors: Current and future trends," pp. 491–500, sep 2012.

[9] M. Roth and L. Rakers, "Intraoperative Neuromonitoring: Principles and Considerations for Perioperative Nurses," *AORN Journal*, vol. 110, no. 1, pp. 11–26, jul 2019.

[10] W. Ishida, J. Casaos, A. Chandra, A. D'Sa, S. Ramhmdani, A. Perdomo-Pantoja, N. Theodore, G. Jallo, Z. L. Gokaslan, J. P. Wolinsky, D. M. Sciubba, A. Bydon, T. F. Witham, and S. F. L. Lo, "Diagnostic and therapeutic values of intraoperative electrophysiological neuromonitoring during resection of intradural extramedullary spinal tumors: A single-center retrospective cohort and meta-analysis," *Journal of Neurosurgery: Spine*, vol. 30, no. 6, pp. 839–849, jun 2019.

[11] P. J. Basser, S. Pajevic, C. Pierpaoli, J. Duda, and A. Aldroubi, "In Vivo Fiber Tractography Using DT-MRI Data," Tech. Rep., 2000.

[12] R. Ito, S. Mori, and E. R. Melhem, "Diffusion tensor brain imaging and tractography," *Neuroimaging Clinics of North America*, vol. 12, no. 1, pp. 1–19, 2002, diffusion Imaging.

[13] D. Stein, Y. Assaf, G. Dar, H. Cohen, V. Slon, E. Kedar, B. Medlej, J. Abbas, O. Hay, D. Barazany, and I. Hershkovitz, "3D virtual reconstruction and quantitative assessment of the human intervertebral disc's annulus fibrosus: a DTI tractography study," *Scientific Reports*, vol. 11, 2021.

[14] C. N. Sigl J.C., "Introduction bispectral analysis Electroencephalogram," 1994.

[15] C. R. D. Oliveira, W. M. Bernardo, and V. M. Nunes, "Benefit of general anesthesia monitored by bispectral index compared with monitoring guided only by clinical parameters. Systematic review and meta-analysis," *Brazilian Journal of Anesthesiology (English Edition)*, vol. 67, no. 1, pp. 72–84, jan 2017.

[16] C. Rosow and P. J. Manberg, "Bispectral Index monitoring," *Anesthesiology Clinics of North America*, vol. 19, no. 4, pp. 947–966, 2001.

[17] F. Scholkmann, S. Kleiser, A. J. Metz, R. Zimmermann, J. Mata Pavia, U. Wolf, and M. Wolf, "A review on continuous wave functional near-infrared spectroscopy and imaging instrumentation and methodology," pp. 6–27, jan 2014.

[18] M. Ferrari and V. Quaresima, "A brief review on the history of human functional near-infrared spectroscopy (fNIRS) development and fields of application," pp. 921–935, nov 2012.

[19] R. Aaslid, T.-M. Markwalder, and H. Nornes, "Noninvasive transcranial doppler ultrasound recording of flow velocity in basal cerebral arteries," *Journal of Neurosurgery*, vol. 57, no. 6, 01 Jan. 1982.

[20] H. L. Edmonds, M. R. Isley, T. B. Sloan, A. V. Alexandrov, and A. Y. Razumovsky, "American Society of Neurophysiologic Monitoring and American Society of Neuroimaging Joint Guidelines for Transcranial Doppler Ultrasonic Monitoring," *Journal of Neuroimaging*, vol. 21, no. 2, pp. 177–183, apr 2011.

[21] A. Monro, "London medical journal, I. Observation on the features and functions of the nervous system, illustrated with tables." vol. IV, 1783.

[22] G. Kellie, "An Account of the Appearances Observed in the Dissection of Two of Three Individuals Presumed to Have Perished in the Storm of the 3d, and Whose Bodies Were Discovered in the Vicinity of Leith on the Morning of the 4th, November 1821; with Some Reflections on the Pathology of the Brain: Part I." *Transactions. Medico-Chirurgical Society of Edinburgh*, vol. 1, no. November, pp. 84–122, 1824.

[23] M. H. Wilson, "Monro-Kellie 2.0: The dynamic vascular and venous pathophysiological components of intracranial pressure," pp. 1338–1350, aug 2016.

[24] J. Hall and M. Hall, *Guyton and Hall Textbook of Medical Physiology*. Elsevier, 2021.

[25] N. Lundberg, "Continuous Recording and Control of Ventricular Fluid Pressure in Neurosurgical Practice," *Journal of Neuropathology Experimental Neurology*, vol. 21, no. 3, pp. 489–489, 07 1962.

[26] ——, "The saga of the monro-kellie doctrine," in *Intracranial Pressure V*, S. Ishii, H. Nagai, and M. Brock, Eds. Berlin, Heidelberg: Springer Berlin Heidelberg, 1983, pp. 68–76.

[27] E. Kandel, S. Mack, T. Jessell, J. Schwartz, S. Siegelbaum, and A. Hudspeth, *Principles of Neural Science, Fifth Edition*, ser. McGraw-Hill's AccessMedicine. McGraw-Hill Education, 2015.

[28] E. Marcolini, C. Stretz, and K. M. DeWitt, "Intracranial hemorrhage and intracranial hypertension," *Emergency Medicine Clinics of North America*, vol. 37, no. 3, pp. 529–544, 2019, critical Care in the Emergency Department.

[29] Z. Czosnyka and M. Czosnyka, "Long-term monitoring of intracranial pressure in normal pressure hydrocephalus and other csf disorders," *Acta Neurochirurgica*, 07 2017.

[30] D. S. Nag, S. Sahu, A. Swain, and S. Kant, "Intracranial pressure monitoring: Gold standard and recent innovations," pp. 1535–1553, jul 2019.

[31] A. K. Filis, K. Aghayev, and F. D. Vrionis, "Cerebrospinal fluid and hydrocephalus: Physiology, diagnosis, and treatment," *Cancer Control*, vol. 24, no. 1, pp. 6–8, 2017, pMID: 28178707.

[32] T. Schizodimos, V. Soulountsi, C. Iasonidou, and N. Kapravelos, "An overview of management of intracranial hypertension in the intensive care unit," pp. 741–757, oct 2020.

[33] J. D. Robinson, "Management of Refractory Intracranial Pressure," pp. 67–75, 2016.

[34] M. Harary, R. G. Dolmans, and W. B. Gormley, "Intracranial pressure monitoring—review and avenues for development," feb 2018.

[35] R. Ma, D. Rowland, A. Judge, A. Calisto, J. Jayamohan, D. Johnson, P. Richards, S. Magdum, and S. Wall, "Complications following intracranial pressure monitoring in children: A 6-year single-center experience," *Journal of Neurosurgery: Pediatrics*, vol. 21, no. 3, pp. 278–283, mar 2018.

[36] S. Tavakoli, G. Peitz, W. Ares, S. Hafeez, and R. Grandhi, "Complications of invasive intracranial pressure monitoring devices in neurocritical care," *Neurosurgical Focus*, vol. 43, no. 5, nov 2017.

[37] J. Vaquero, R. J. Fontana, A. M. Larson, N. M. Bass, T. J. Davern, A. O. Shakil, S. Han, M. E. Harrison, T. R. Stravitz, S. Muñoz, R. Brown, W. M. Lee, and A. T. Blei, "Complications and use of intracranial pressure monitoring in patients with acute liver failure and severe encephalopathy," *Liver Transplantation*, vol. 11, no. 12, pp. 1581–1589, dec 2005.

[38] A. A. Rabinstein, "Treatment of Brain Edema in Acute Liver Failure," pp. 129–141, mar 2010.

[39] A. T. Blei, "Brain edema in acute liver failure: can it be prevented? can it be treated?" *Journal of hepatology*, vol. 46, no. 4, pp. 564–569, 2007.

[40] S. Agerskov, M. Wallin, P. Hellström, D. Ziegelitz, C. Wikkelsö, M. Tullberg, and S. Agerskov, "Absence of disproportionately enlarged subarachnoid space hydrocephalus, a sharp callosal angle, or other morphologic MRI markers should not be used to exclude patients with idiopathic normal pressure hydrocephalus from shunt surgery," *American Journal of Neuroradiology*, vol. 40, no. 1, pp. 74–79, jan 2019.

[41] J. Bellner, B. Romner, P. Reinstrup, K. A. Kristiansson, E. Ryding, and L. Brandt, "Transcranial Doppler sonography pulsatility index (PI) reflects intracranial pressure (ICP)," *Surgical Neurology*, vol. 62, no. 1, pp. 45–51, jul 2004.

[42] A. D'Andrea, M. Conte, M. Cavallaro, R. Scarafile, L. Riegler, R. Cocchia, E. Pezzullo, A. Carbone, F. Natale, G. Santoro, P. Caso, M. G. Russo, E. Bossone, and R. Calabrò, "Transcranial Doppler ultrasonography: From methodology to major clinical applications," *World Journal of Cardiology*, vol. 8, no. 7, p. 383, 2016.

[43] C. Hylkema, "Optic Nerve Sheath Diameter Ultrasound and the Diagnosis of Increased Intracranial Pressure," pp. 95–99, 2016.

[44] C. Robba, G. Santori, M. Czosnyka, F. Corradi, N. Bragazzi, L. Padayachy, F. S. Taccone, and G. Citerio, "Optic nerve sheath diameter measured sonographically as non-invasive estimator of intracranial pressure: a systematic review and meta-analysis," pp. 1284–1294, aug 2018.

[45] C. M. Campbell-Bell, A. A. Birch, D. Vignali, D. Bulters, and R. J. Marchbanks, "Reference intervals for the evoked tympanic membrane displacement measurement: A non-invasive measure of intracranial pressure," *Physiological Measurement*, no. 1, p. 19, jan 2018.

[46] W. K. El-Bouri, D. Vignali, K. Iliadi, D. Bulters, R. J. Marchbanks, A. A. Birch, and D. M. Simpson, "Quantifying the contribution of intracranial pressure and arterial blood pressure to spontaneous tympanic membrane displacement," *Physiological Measurement*, vol. 39, no. 8, aug 2018.

[47] S. Oliveira, G. H. F. Vilela, C. Carlotti, L. Damiano, W. Seluque, B. Colli, K. Tanaka, C. Wang, and K. Nonaka, "The new icp minimally invasive method shows that the monro–kellie doctrine is not valid," *Acta neurochirurgica. Supplement*, vol. 114, pp. 117–20, 01 2012.

[48] D. Felten, M. O'Banion, and M. Maida, *Netter's Atlas of Neuroscience*, ser. Netter Basic Science. Elsevier, 2014.

[49] M. Siqueira, *Tratado De Neurocirurgia*. Manole, 2015.

[50] N. Carney, A. M. Totten, J. S. Ullman, G. W. J. Hawryluk, M. J. Bell, S. L. Bratton, R. Chesnut, O. A. Harris, A. M. Rubiano, R. C. Tasker, M. S. Vavilala, J. Wilberger, D. W. Wright, and J. Ghajar, "Guidelines for the Management of Severe Traumatic Brain Injury 4th Edition," Tech. Rep., 2016.

[51] R. D. Stevens, M. Shoykhet, and R. Cadena, "Emergency Neurological Life Support: Intracranial Hypertension and Herniation," pp. 76–82, dec 2015.

[52] A. C. of Surgeons. Committee on Trauma, *Advanced Trauma Life Support: ATLS Student Course Manual*. American College of Surgeons, 2018.

[53] A. Meyer, "Herniation of the brain," Tech. Rep., 1920.

[54] A. Marmarou, K. Shulman, and J. LaMorgese, "Compartmental analysis of compliance and outflow resistance of the cerebrospinal fluid system," *Journal of Neurosurgery*, vol. 43, no. 5, 01 Jan. 1975.

[55] C. Hawthorne and I. Piper, "Monitoring of intracranial pressure in patients with traumatic brain injury," *Frontiers in neurology*, vol. 5, p. 121, 2014.

[56] M. Czosnyka and Z. Czosnyka, "Origin of intracranial pressure pulse waveform," *Acta Neurochirurgica*, vol. 162, no. 8, pp. 1815–1817, 2020.

[57] K. B. Evensen, K. Paulat, F. Prieur, S. Holm, and P. K. Eide, "Utility of the Tympanic Membrane Pressure Waveform for Non-invasive Estimation of The Intracranial Pressure Waveform," *Scientific Reports*, vol. 8, no. 1, dec 2018.

[58] K. Evensen and P. Eide, "Mechanisms behind altered pulsatile intracranial pressure in idiopathic normal pressure hydrocephalus: role of vascular pulsatility and systemic hemodynamic variables," *Acta Neurochirurgica*, vol. 162, no. 8, pp. 1803–1813, aug 2020.

[59] P. K. Eide and W. Sorteberg, "Intracranial pressure levels and single wave amplitudes, Glasgow Coma Score and Glasgow Outcome Score after subarachnoid haemorrhage," *Acta Neurochirurgica*, vol. 148, no. 12, pp. 1267–1275, dec 2006.

[60] M. D. Okon, C. J. Roberts, A. M. Mahmoud, A. N. Springer, R. H. Small, J. M. McGregor, and S. E. Katz, "Characteristics of the cerebrospinal fluid pressure waveform and craniospinal compliance in idiopathic intracranial hypertension subjects," *Fluids and Barriers of the CNS*, vol. 15, no. 1, aug 2018.

[61] E. Carrera, D.-J. Kim, G. Castellani, C. Zweifel, Z. Czosnyka, M. Kasprowicz, P. Smielewski, J. D. Pickard, and M. Czosnyka, "What Shapes Pulse Amplitude of Intracranial Pressure?" *Journal fo Neurotrauma*, vol. 27, pp. 317–324, feb 2010.

[62] X. Hu, P. Xu, F. Scalzo, P. Vespa, and M. Bergsneider, "Morphological clustering and analysis of continuous intracranial pressure," *IEEE Transactions on Biomedical Engineering*, vol. 56, no. 3, pp. 696–705, 2008.

[63] I. Martinez-Tejada, A. Arum, J. E. Wilhjelm, M. Juhler, and M. Andresen, "B waves: A systematic review of terminology, characteristics, and analysis methods," oct 2019.

[64] "2000_KIRKNESS_ICP waveform analysis-clinical research implications."

[65] E. R. Cardoso, J. O. Rowan, and S. P. Galbraith, "Analysis of the cerebrospinal fluid pulse wave in intracranial pressure," Tech. Rep., 1983.

[66] "ANALYSIS OF INTRACRANIAL PRESSURE," Tech. Rep., 1992.

[67] K. Germon, "Interpretation of icp pulse waves to determine intracerebral compliance." *The Journal of neuroscience nursing: journal of the American Association of Neuroscience Nurses*, vol. 20, no. 6, pp. 344–351, 1988.

[68] J. Arroyo-Palacios, M. Rudz, R. Fidler, W. Smith, N. Ko, S. Park, Y. Bai, and X. Hu, "Characterization of Shape Differences Among ICP Pulses Predicts Outcome of External Ventricular Drainage Weaning Trial," *Neurocritical Care*, vol. 25, no. 3, pp. 424–433, dec 2016.

[69] O. Hirai, H. Handa, M. Ishikawa, and S.-H. Kim, "Epidural pulse waveform as an indicator of intracranial pressure dynamics," *Surgical neurology*, vol. 21, no. 1, pp. 67–74, 1984.

[70] T. TOKUTOMI, M. SHIGEMORI, T. YUGE, F. YAMAMOTO, M. WATANABE, S. KURAMOTO, and S. GOTO, "Analysis of pulse wave recorded on epidural pressure in acute intracranial hypertension," *Neurologia medico-chirurgica*, vol. 25, no. 6, pp. 418–424, 1985.

[71] M. Shigemori, T. Tokutomi, T. Kawaba, H. Nakashima, and S. Kuramoto, "Analysis of epidural pressure pulse wave (edp-pw) and common carotid blood velocity (cbfv) in acute intracranial hypertension," *Neurological research*, vol. 8, no. 2, pp. 105–108, 1986.

[72] M. SHIGEMORI, T. KAWABA, T. TOKUTOMI, H. NAKASHIMA, T. YUGE, and S. KURAMOTO, "Analysis of pulse waves of epidural pressure recorded in acute intracranial hypertension amplitude changes of pulse wave components and their clinical significance," *Neurologia medico-chirurgica*, vol. 27, no. 4, pp. 289–294, 1987.

[73] P. K. Eide, "Assessment of childhood intracranial pressure recordings using a new method of processing intracranial pressure signals," *Pediatric neurosurgery*, vol. 41, no. 3, pp. 122–130, 2005.

[74] R. Andrade, "Analysis and improvement of a non-invasive intracranial pressure monitoring system," Master's thesis, 2013.

[75] G. H. F. Vilela, B. Cabella, S. Mascarenhas, M. Czosnyka, P. Smielewski, C. Dias, D. A. Cardim, C. C. Wang, P. Mascarenhas, R. Andrade, K. Tanaka, L. S. Lopes, and B. O. Colli, "Validation of a new noninvasive intracranial pressure monitoring method by direct comparison with an invasive technique," *Acta Neurochirurgica, Supplementum*, vol. 122, pp. 93–96, 2016.

[76] B. Cabella, G. H. F. Vilela, S. Mascarenhas, M. Czosnyka, P. Smielewski, C. Dias, D. A. Cardim, C. C. Wang, P. Mascarenhas, R. Andrade, K. Tanaka, L. d. S. Lopes, and B. O. Colli, *Validation of a new noninvasive intracranial pressure monitoring method by direct comparison with an invasive technique*. Springer, 2016.

[77] G. Frigieri, R. A. P. Andrade, C. Dias, D. L. Spavieri, R. Brunelli, D. A. Cardim, C. C. Wang, R. M. Verzola, and S. Mascarenhas, "Analysis of a non-invasive intracranial pressure monitoring method in patients with traumatic brain injury," *Acta Neurochirurgica, Supplementum*, vol. 126, pp. 107–110, 2018.

[78] G. H. F. Vilela, "Development of a minimally invasive system to monitor the intracranial pressure." Ph.D. dissertation, 2010.

[79] "Ansi/aami bp22:1994 (r)2016 blood pressure transducer," American National Standard, Geneva, CH, Standard, 2016.

[80] B. Lindquist, E. Fernell, E.-K. Persson, and P. Uvebrant, "Quality of life in adults treated in infancy for hydrocephalus," *Child's Nervous System*, vol. 30, no. 8, pp. 1413–1418, 2014.

[81] V. L. Feigin, T. Vos, E. Nichols, M. O. Owolabi, W. M. Carroll, M. Dichgans, G. Deuschl, P. Parmar, M. Brainin, and C. Murray, "The global burden of neurological disorders: translating evidence into policy," *The Lancet Neurology*, vol. 19, no. 3, pp. 255–265, 2020.

[82] M. Torbey, R. Geocadin, A. Razumovsky, D. Rigamonti, and M. Williams, "Utility of csf pressure monitoring to identify idiopathic intracranial hypertension without papilledema in patients with chronic daily headache," *Cephalalgia*, vol. 24, no. 6, pp. 495–502, 2004.

[83] M. Togha, K. Shirbache, R. Rahmanzadeh, Z. Ghorbani, Z. Yari, F. Refaeian, S. Behbahani, and P. Panahi, "Prevalence of new-onset migraine in patients with idiopathic intracranial hypertension in comparison to the general population," *Iranian journal of neurology*, vol. 17, no. 4, p. 161, 2018.

[84] R. E. Ryan Jr and S. H. Pearlman, "Common headache misdiagnoses." *Primary care*, vol. 31, no. 2, pp. 395–405, 2004.

[85] E. B. Lee, F. S. Edelman, and C. E. Stafstrom, "Evidence of diplopia in children's headache drawings helps to differentiate pseudotumor cerebri from migraine," *Pediatric neurology*, vol. 79, pp. 40–44, 2018.

[86] R. M. Mallery, D. I. Friedman, and G. T. Liu, "Headache and the pseudotumor cerebri syndrome," *Current pain and headache reports*, vol. 18, no. 9, p. 446, 2014.

[87] J. S. Lawley, L. G. Petersen, E. J. Howden, S. Sarma, W. K. Cornwell, R. Zhang, L. A. Whitworth, M. A. Williams, and B. D. Levine, "Effect of gravity and microgravity on intracranial pressure," *The Journal of physiology*, vol. 595, no. 6, pp. 2115–2127, 2017.

[88] K.-i. Iwasaki, Y. Ogawa, T. Kurazumi, S. M. Imaduddin, C. Mukai, S. Furukawa, R. Yanagida, T. Kato, T. Konishi, A. Shinojima *et al.*, "Long-duration spaceflight alters estimated intracranial pressure and cerebral blood velocity," *The Journal of physiology*, vol. 599, no. 4, pp. 1067–1081, 2021.

[89] D. Alexander, C. Gibson, D. Hamilton, S. Lee, T. Mader, C. Otto, C. Oubre, A. Pass, S. Platts, J. Scott *et al.*, "Nasa evidence report: Risk of spaceflight-induced intracranial hypertension and vision alterations," 2012.

Rodrigo de A. P. Andrade received the B.S. degree in control and automation engineering from Centro Federal de Educação Tecnológica de Minas Gerais, Leopoldina, Brazil, in 2010 and the M.S. degree in mechanical engineering from University of São Paulo, São Carlos, Brazil, in 2013. He is currently pursuing the Ph.D. degree in electrical engineering at University of São Paulo, São Carlos, Brazil. He is co-founder, currently Responsible Engineer in Charge and product development director at Braincare Desenvolvimento e Inovação Tecnológica S.A. working on the development of medical products. Has experience in medical devices, industrial automation, with an emphasis on embedded instrumentation, acting mainly on the following topics: Medical instrumentation, sensors, wireless data acquisition, optogenetic instrumentation and automated test systems development.

Helder Eiki Oshiro received the B.S. degrees in electrical engineering from the Federal University of São Carlos (UFSCar), São Carlos, in 2019. Since 2017, he has been working at Braincare Desenvolvimento e Inovação Tecnológica S.A. in the engineering team and is currently pursuing a M.S. degree in Electrical Engineering at the University of São Paulo (USP), São Carlos, Brazil.

Caio Kioshi Miyazaki received the B.S. degree in electrical engineering from University of São Paulo, São Carlos, Brazil, in 2017. He is currently pursuing the M.S. degree in electrical engineering from University of São Paulo, São Carlos, Brazil and he is working in product development at Braincare Desenvolvimento e Inovação Tecnológica S.A.

Cintya Yukie Hayashi received the B.S. degree in Nursing from School of Nursing at University of Sao Paulo, Sao Paulo, Brazil, in 2011; participated in the International Junior Year Abroad Programme (Adult Nursing) at the School of Healthcare, University of Leeds, Leeds, UK, in 2009; received the Cardiology Nurse Specialist degree from the Heart Institute of Hospital das Clinicas da Faculdade de Medicina da USP, University of Sao Paulo, Sao Paulo, Brazil, in 2013; and the M.S. degree in Neurosciences from Faculty of Medicine at University of Sao Paulo, Sao Paulo, Brazil, in 2018. She is currently Clinical Research Nurse Coordinator at Braincare Desenvolvimento e Inovação Tecnológica S.A., Brazil, and also pursuing the Ph.D. degree in Neurosciences at University of Sao Paulo, Sao Paulo, Brazil. From 2013 to 2015 was course coordinator at Brazilian Committee on Trauma for Advanced Trauma Life Support programme in Brazil and Latin America in partnership with the American College of Surgeons. From 2012 to 2013 worked as a registered nurse at the Emergency Department of University of Sao Paulo Hospital.

Marcos Antonio de Morais , received System Analysis and Development degree from Federal Institute of São Paulo-IFSP, São Carlos, Brazil, in 2012. Has experience in development of automation systems, supervised softwares, manufacturer control, design and assembly of electrical panels, integration of equipment and instrumentation. Responsible for development and implementation test procedures of products at Braincare Desenvolvimento e Inovação Tecnológica S.A.

Rodrigo Brunelli received the B.S. degree in Computational Physics from the University of São Paulo, São Carlos, Brazil, in 2013. He currently works as a quality assurance manager and leader in the firmware developer embedded systems at Braincare Desenvolvimento e Inovação Tecnológica S.A. He has experience with medical devices and embedded systems, working on the following topics: medical instrumentation, sensors, serial and wireless communications and software quality.

João Paulo Carmo obtained the PhD degree on Industrial Electronics. He is Professor in the University of São Paulo (USP) in São Carlos SP, Brazil. He is involved in the research on micro/nano-technologies, solid-state integrated sensors, and microdevices for biomedical and industrial applications. Professor Carmo is also vice-director of the Group of Metamaterials, Microwaves and Optics (GMeta).